

Label-efficient Single Photon Images Classification via Active Learning

ZILI ZHANG,^{1,†} ZITING WEN,^{2,†} YIHENG QIANG,¹ HONGZHOU DONG,¹
WENLE DONG,¹ XINYANG LI,¹ XIAOFAN WANG,^{1,3} AND XIAOQIANG
REN,^{1,*}

¹*School of Mechatronic Engineering and Automation, Shanghai University, Shanghai 200444, China*

²*Australian Center for Robotics, School of Aerospace, Mechanical and Mechatronic Engineering, the University of Sydney, NSW 2006, Sydney*

³*Shanghai Institute of Technology, Shanghai 200235, China*

[†]*These authors contributed equally to this work.*

*xqren@shu.edu.cn

Abstract:

Single-photon LiDAR achieves high-precision 3D imaging in extreme environments through quantum-level photon detection technology. Current research primarily focuses on reconstructing 3D scenes from sparse photon events, whereas the semantic interpretation of single-photon images remains underexplored, due to high annotation costs and inefficient labeling strategies. This paper presents the first active learning framework for single-photon image classification. The core contribution is an imaging condition-aware sampling strategy that integrates synthetic augmentation to model variability across imaging conditions. By identifying samples where the model is both uncertain and sensitive to these conditions, the proposed method selectively annotates only the most informative examples. Experiments on both synthetic and real-world datasets show that our approach outperforms all baselines and achieves high classification accuracy with significantly fewer labeled samples. Specifically, our approach achieves 97% accuracy on synthetic single-photon data using only 1.5% labeled samples. On real-world data, we maintain 90.63% accuracy with just 8% labeled samples, which is 4.51% higher than the best-performing baseline. This illustrates that active learning enables the same level of classification performance on single-photon images as on classical images, opening doors to large-scale integration of single-photon data in real-world applications.

1. Introduction

Single-photon LiDAR is a cutting-edge optoelectronic technology that leverages quantum detection techniques by emitting individual photons and employing ultra-sensitive single-photon detectors [1–3]. This technology enables micrometer-level target detection and precise three-dimensional imaging even under extreme operational conditions, such as ultra-long distances, haze, and smoke, while requiring only milliwatt-level laser power [4–8]. Its advantages of compact size, lightweight design, and ultra-low power consumption make it particularly suitable for deployment in platforms such as micro unmanned aerial vehicles, unmanned surface vessels, and low-orbit satellites, supporting applications including underwater exploration, atmospheric aerosol monitoring, and biomedical imaging [9–12].

Recent progress in single-photon imaging has largely focused on recovering high-fidelity depth and intensity maps from sparse photon returns, employing statistical and computational tools such as Poisson modeling, compressed sensing, and machine learning [13–16]. However, most existing work stops at the reconstruction task, and semantic interpretation of single-photon images remains unexplored. Developing classification and detection models for these images is a key step toward realizing single-photon imaging as a complete sensing system [17, 18].

Deep neural networks have achieved remarkable performance in semantic understanding tasks such as classification and detection, but their success relies heavily on the availability of large-

scale annotated datasets, exemplified by RGB-based datasets like ImageNet [19]. Unfortunately, creating such datasets in single-photon settings is extremely costly. The inherent challenges of low resolution, stochastic noise, and detector imperfections substantially increase the burden of manual annotation, making it difficult to construct large-scale labeled datasets. As a result, current methods typically rely on small, randomly labeled subsets, which limit model performance due to inefficient use of labeling resources [20, 21].

Active learning offers a promising solution to reduce annotation costs by identifying and labeling only the most informative samples, and has been extensively explored in the context of RGB image tasks [22, 23]. Existing active learning strategies can be broadly categorized into three groups: uncertainty-based, diversity-based, and hybrid approaches. Uncertainty-based methods select samples on which the model is least confident, typically measured using entropy [24] or prediction margin [25]. Diversity-based methods focus on selecting samples that are dissimilar from the already labeled set in the feature space, aiming to ensure broad coverage of the data distribution [26]. Hybrid strategies combine the strengths of both, for example by performing diversity sampling in the gradient embedding space, as in BADGE [27], to acquire samples that are both uncertain and representative.

However, these methods typically operate under the assumption that each sample is fully characterized by a single observation. This assumption does not hold in single-photon imaging. In single-photon systems, each image is inherently affected by stochastic noise and variable imaging conditions, such as fluctuations in photon counts and signal-to-background ratios. As a result, a sample that appears confidently classified under one condition may become highly uncertain under another. Conventional methods, which ignore this variability, may therefore misestimate sample informativeness and select suboptimal samples for annotation.

To address this gap, this paper proposes a novel active learning framework tailored to single-photon image classification. Drawing inspiration from recent advances in optical imaging, such as the use of synthetic data to support model training [28] and uncertainty estimation to evaluate imaging system robustness [29], we extend these ideas into the setting of single-photon image classification with limited labels. The core innovation of our approach lies in embedding imaging condition-aware synthetic augmentation into the active learning loop and introducing an uncertainty-inconsistency sampling strategy. For each observed single-photon image, we simulate multiple variants under diverse imaging conditions. By evaluating prediction consistency across these variants, our method prioritizes samples where the model is both uncertain and sensitive to imaging variations. This targeted selection strategy enables more efficient model training under limited labels. Experiments on both synthetic and self-collected real-world datasets demonstrate that our method outperforms all baseline methods. It achieves high classification accuracy with substantially fewer labeled samples, highlighting its potential for enabling scalable and label-efficient semantic understanding in single-photon sensing applications.

The rest of this paper is organized as follows. Section 2 presents the novel active learning approach in detail, Section 3 experimentally validates the effectiveness of our approach, and Section 4 concludes the paper with a summary of key findings.

2. Method

2.1. Single Photon Imaging System and Method

Single-Photon LiDAR is an advanced sensing device grounded in quantum detection principles, integrating several critical components: a single-photon avalanche diode (SPAD), a laser source, a micro-electromechanical system (MEMS) scanning mirror, and a time-correlated single-photon counting module (TCSPC), as shown in Figure 1. The operational principle of the system begins with the periodic emission of pulsed laser beams, which are precisely controlled in terms of energy parameters. The emission angle of the laser beam is meticulously managed by the MEMS scanning mirror, facilitating point-by-point scanning of the target region. When the pulsed laser

beam illuminates the target object, the SPAD detects the extremely faint optical radiation signals reflected from the target, which have power levels as low as femtowatts or below. These detected photon events are subsequently converted into time-tagged electrical signal pulses by the TCSPC module. The time-digital processing module then performs temporal distribution statistics on the discrete photon events, constructing photon-counting histograms for each pixel.

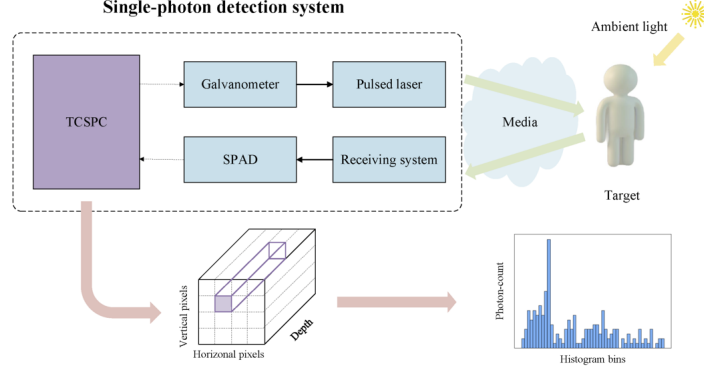


Fig. 1. Single-Photon Imaging System Components.

The obtained photon-counting histogram can be defined as a three-dimensional tensor $\mathbf{N} \in \mathbb{Z}_+^{N_r \times N_c \times T}$, where $N_r \times N_c$ represents the pixel and T is the number of histogram bins. Each element $n_{i,j,t}$ records the number of photons detected by pixel $(i, j) \in [1, N_r] \times [1, N_c]$ in the $t \in [1, T]$ time bin, which follows the Poisson distribution:

$$n_{i,j,t} \sim \mathcal{P}(\lambda_{i,j,t}(\mathbf{I}, \mathbf{a}, \mathbf{b})), \quad (1)$$

where $\mathbf{I} \in \mathbb{R}_+^{N_r \times N_c}$ is the lidar depth values, $\mathbf{a} \in \mathbb{R}_+^{N_r \times N_c}$ represents the intensity values, and $\mathbf{b} \in \mathbb{R}_+^{N_r \times N_c}$ is the background level. $\lambda_{i,j,t}$ represents the theoretical photon count and can be expressed by the following physical model:

$$\lambda_{i,j,t} = g_{i,j} \left[\sum_{i,j} a_{i,j} h_{i,j}(t - t_{i,j}^d) + b_{i,j} \right], \quad (2)$$

where $h_{i,j}(\cdot)$ is the known temporal instrumental response (dependent on the system) per pixel, $b_{i,j}$ is the background level in pixel (i, j) , $a_{i,j}$ is the reflectivity in pixel (i, j) , $t_{i,j}^d$ represents the time bin corresponding to the true depth $I_{i,j}$, and $g_{i,j}$ is a scaling factor representing the gain/sensitivity of the detector.

Assuming mutual independence between the noise realizations in different time bins and pixels, the negative log-likelihood function associated with the observations $n_{i,j,t}$ can be written as:

$$g(\mathbf{I}, \mathbf{a}, \mathbf{b}) = - \sum_{i=1}^{N_c} \sum_{j=1}^{N_r} \sum_{t=1}^T \log p(n_{i,j,t} | \mathbf{I}, \mathbf{a}, b_{i,j}), \quad (3)$$

where $p(n_{i,j,t} | \mathbf{I}, \mathbf{a}, b_{i,j})$ is the probability mass associated with the Poisson distribution.

This function contains all the information associated with the observation model. By solving this optimization problem, the depth and intensity information of the target can be obtained.

2.2. Active Learning Framework

Active learning is an effective strategy for reducing annotation costs by selectively querying labels for the most informative samples [23]. Rather than randomly annotating data, it aims to identify those samples that are expected to most improve model performance, based on the assumption that not all data points contribute equally to learning.

In the context of single-photon imaging, we adapt this principle by incorporating imaging condition-aware synthetic augmentation into the active learning process. Our framework evaluates each sample under diverse simulated conditions and uses this information to quantify both prediction uncertainty and sensitivity to imaging variations. These estimates guide a sampling strategy that selects the most impactful samples for labeling, enabling efficient model improvement with limited supervision.

In our active learning framework, we define four data pools and a model as follows. The labeled dataset is denoted as $D_l = \{(I_{\text{obs},i}, y_i)\}_{i=1}^{N_l}$, where $I_{\text{obs},i}$ represents the i -th observed single-photon depth image with its label y_i , and N_l is the total number of labeled samples. The unlabeled dataset is denoted as $D_u = \{I_{\text{obs},i}\}_{i=1}^{N_u}$, which consists of N_u unlabeled observed images.

To improve the robustness of the model and the reliability of uncertainty estimation, we expand both the labeled and unlabeled datasets by generating multiple synthetic images for each observed sample under varying photon count conditions. Specifically, for each observed image $I_{\text{obs},i}$, we define a sample group $S_i = \{I_{\text{obs},i}\} \cup \{I_{\text{syn},i,j}\}_{j=1}^M$, where M denotes the number of synthetic images associated with $I_{\text{obs},i}$. Using this notation, the extended labeled dataset and extended unlabeled dataset are expressed as $D'_l = \{(S_i, y_i)\}_{i=1}^{N_l}$, $D'_u = \{S_i\}_{i=1}^{N_u}$.

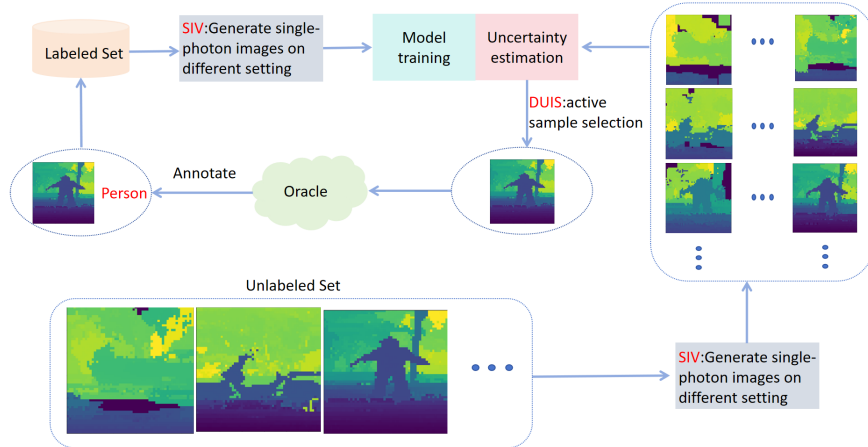


Fig. 2. Framework: In each active learning iteration, we first train the model on the current labeled dataset, augmented with synthetic single-photon images under varying conditions by the synthetic imaging variants (SIV) module. We then estimate uncertainty based on model predictions across these synthetic images. The most uncertain samples from the unlabeled dataset are selected by diversity-guided uncertainty-inconsistency sampling strategy (DUI) and sent to the Oracle for labeling. The newly labeled samples are added to the training set. This process repeats until the labeling budget is exhausted.

The overall framework is shown in Figure 2. The model $f_\theta(\cdot)$ is initially trained on D'_l , leveraging both observed and synthetic images to improve generalization. The active learning

Algorithm 1: Synthetic Data Generation for Single-Photon Imaging

Input: Depth ground truth I_{obs} , normalized reflectance ground truth \hat{A}_{obs} , mean signal photons per pixel \hat{z}_{sig} , time bin duration Δt , pulse root mean square width T_{pulse} , the time bin corresponding to the maximum detection distance t_{BinMax}

Output: Synthetic single-photon imaging I_{syn}

foreach *pixel* (i, j) **do**

- Compute time bins:** $t_{\text{obs}} \leftarrow \text{Eq.4}$
- Generate Signal Photons:** $n_{\text{sig}}(i, j) \leftarrow \text{Eq.6}; t_{\text{sig}}(i, j) \leftarrow \text{Eq.5}.$
- Generate Background Noise:** $n_{\text{bg}}(i, j) \leftarrow \text{Eq.7}; t_{\text{bg}}(i, j) \leftarrow \text{Eq.8}.$
- Generate Simulated Single-Photon Raw Data:** Combine the generated signal detection times and background light detection times: $\mathcal{S} \leftarrow t_{\text{sig}}(i, j) \cup t_{\text{bg}}(i, j).$
- Generate Synthetic Single-Photon Imaging:** Input the raw single-photon data into the sparse single-photon imaging network $I_{\text{syn}} \leftarrow \text{SSPI}(\mathcal{S})$

return $I_{\text{syn}}.$

process then proceeds iteratively, selecting a batch of the most valuable sample groups for labeling. At each iteration, the model evaluates the uncertainty and inconsistency of each sample group S_i in the unlabeled dataset D'_u , rather than individual observed images $I_{\text{obs},i}$. By processing multiple synthetic variants within each group and aggregating their predictions, the model captures variations in the imaging process, leading to a more reliable estimate compared to relying on a single observed image.

Based on the estimated uncertainty and inconsistency, a batch of the most valuable sample groups is selected and sent to the oracle for labeling. The newly labeled observed images are incorporated into D_l , and their corresponding synthetic augmentations are added to D'_l . The model $f_\theta(\cdot)$ is then retrained on the updated dataset. This process repeats iteratively until the labeling budget is exhausted.

Throughout this framework, synthetic images serve a dual purpose: they enrich the training data D'_l and strengthen the uncertainty estimation procedure that guides active learning. The result is an efficient training loop where $f_\theta(\cdot)$ improves by focusing labeling effort on valuable samples.

2.3. Generating Multi-Condition Single-Photon Images

The uncertainty in single-photon imaging primarily stems from the effects of stochastic photon statistics. Photon arrival statistics inherently follow a Poisson distribution, where the variance equals the photons per pixel (PPP). Under low photon count conditions, the timestamp resolution of TCSPC is limited, leading to increased depth measurement errors. Additionally, the absence of photon arrivals in certain pixels (PPP ≈ 0) results in data gaps, causing voids in the reconstructed depth map.

To generate single-photon data under varying conditions, we first configure the detector's physical parameters, including the time bin duration Δt and pulse root mean square width T_{pulse} . The depth ground truth I_{obs} is then converted into corresponding time bins

$$t_{\text{obs}} = 2I_{\text{obs}} / (c \cdot \Delta t), \quad (4)$$

where c represents the speed of light. The signal detection time t_{sig} is modeled as a Gaussian pulse profile with mean t_{obs} and standard deviation $\sigma = T_{\text{pulse}}/2$

$$t_{\text{sig}} = t_{\text{obs}} + \sigma \cdot \mathcal{N}(0, 1). \quad (5)$$

The number of signal photons n_{sig} follows a Poisson random process described by:

$$n_{\text{sig}} \sim \text{Poisson} \left(N_{\text{pulses}} \cdot \hat{n}_{\text{sig}} \cdot \hat{A}_{\text{obs}} \right), \quad (6)$$

where \hat{n}_{sig} represents the mean signal photons per pixel (MSPPP), \hat{A}_{obs} denotes the normalization parameter derived from the reflectance ground truth, and N_{pulses} denotes the number of pulses required for a pixel to generate one signal photon on average under low-flux conditions.

The background photon count n_{bg} can also be generated via a Poisson distribution based on the predefined signal-to-background ratio (SBR)

$$n_{\text{bg}} \sim \text{Poisson} \left(\frac{\text{mean}(n_{\text{sig}})}{\text{SBR}} \right), \quad (7)$$

where $\text{mean}(n_{\text{sig}})$ represents the average number of signal photons.

According to [30], the background detection time follows the uniform distribution below:

$$t_{\text{bg}} \sim \text{Unif} (0, t_{\text{BinMax}}), \quad (8)$$

where t_{BinMax} represents the time bin corresponding to the maximum detection distance. By mixing the generated signal photons with background photons according to eqs.(5)-(8), the single-photon raw measurements can be obtained. By systematically configuring different system parameters, we generate corresponding synthetic single-photon measurement data. These data are subsequently fed into the sparse single-photon imaging network (SSPI) [31] to reconstruct single-photon images with varying quality levels, effectively emulating the stochastic noise characteristics and uncertainties inherent in single-photon LiDAR systems. The detailed implementation steps are outlined in Algorithm 1.

Algorithm 1 defines the synthetic imaging variants (SIV) module, which plays a central role in enabling uncertainty estimation for single-photon image classification. By systematically varying imaging conditions—mean signal photons per pixel (MSPPP), SIV generates multiple realistic variants from a single observed single-photon image. These variants capture the intrinsic stochasticity of photon measurements and provide the necessary input for estimating both uncertainty and prediction inconsistency in the subsequent active learning process.

2.4. Active Sample Selection

After training the model $f_{\theta}(\cdot)$ on the current labeled dataset D'_l , we select the most informative and diverse samples from D'_u for annotation. The selection process involves computing an uncertainty-inconsistency score for each sample group S_i and a clustering-based selection step to ensure diversity in the batch.

To ensure diversity within each selected batch, we first extract feature representations from the penultimate layer of the trained model $f_{\theta}(\cdot)$. Then, we apply the k-means clustering algorithm to these features to form N_{cand} clusters. A diverse candidate pool is constructed by selecting the sample groups closest to each of these cluster centers.

From this candidate pool, we further assess each group's informativeness by computing an uncertainty-inconsistency score (UIS). This score integrates two aspects: margin-based uncertainty and prediction inconsistency across synthetic variants of each observed image. Specifically, for each image $I \in S_i$, the trained model produces a probability distribution over C possible class labels, denoted as $f_{\theta}(I)$. We denote average model prediction across all images in S_i as \bar{p}_i .

The margin-based uncertainty is defined as the difference between the two highest probabilities in this mean prediction, as shown in eq. 9, where classes c_1 and c_2 have the highest and second-highest predicted probabilities, respectively. A smaller margin indicates higher uncertainty, suggesting that labeling these samples would effectively refine the model's decision boundaries:

Algorithm 2: Active Learning with Uncertainty-Inconsistency Score

Input: Labeled dataset D'_l , unlabeled dataset D'_u , model $f_\theta(\cdot)$, max iterations T , batch size N_{batch} , candidate size N_{cand}

Output: Updated D'_l , updated model $f_\theta(\cdot)$

for $\text{iteration} = 1$ to T **do**

Train Model: Train $f_\theta(\cdot)$ on D'_l .

Diverse Candidate Pool: Extract features from penultimate layer of $f_\theta(\cdot)$ for images in D_u . Apply k-means clustering and select N_{cand} samples closest to cluster centers, forming candidate pool D_{cand} .

Compute Uncertainty-Inconsistency:

foreach $S_i \in D'_u$ **do**

$\bar{p}_i \leftarrow \text{mean}(f_\theta(I)), I \in S_i$; $\text{Margin}(S_i) \leftarrow \text{Eq. 9}$; $\text{Div}_{\text{var}}(S_i) \leftarrow \text{Eq. 10}$;
 $\text{UIS}(S_i) \leftarrow \text{Div}_{\text{var}}(S_i) - \text{Margin}(S_i)$.

Informative Batch Selection: Select top N_{batch} groups from D_{cand} with highest UIS scores to form final selection batch \mathcal{B} ;

Label & Update: Label \mathcal{B} and update $D'_l \leftarrow D'_l \cup \mathcal{B}$, $D'_u \leftarrow D'_u \setminus \mathcal{B}$

return $D'_l, f_\theta(\cdot)$

$$\text{Margin}(S_i) = \bar{p}_i(c_1) - \bar{p}_i(c_2). \quad (9)$$

To quantify the inconsistency across varying imaging conditions, we compute the average KL divergence between each image’s prediction and the mean prediction within S_i as eq. (10). A higher inconsistency indicates sensitivity to imaging conditions, highlighting potential improvements in model robustness from annotating these samples:

$$\text{Div}_{\text{var}}(S_i) = \frac{1}{M+1} \sum_{I \in S_i} D_{\text{KL}}(f_\theta(I) \| \bar{p}_i). \quad (10)$$

Combining these factors, we define the final uncertainty-inconsistency score as eq. 11. Selecting samples with high UIS ensures they are both informative and beneficial for improving model’s robustness. Finally, the selected samples are sent to the oracle for labeling and incorporated into D_l , along with their synthetic augmentations in D'_l :

$$\text{UIS}(S_i) = \text{Div}_{\text{var}}(S_i) - \text{Margin}(S_i). \quad (11)$$

This selection process forms a novel diversity-guided uncertainty-inconsistency sampling strategy (DUIS) that combines representation-level clustering with a task-aware informativeness score. By jointly considering margin-based uncertainty and prediction inconsistency across synthetic variants, DUIS captures both the ambiguity of the model’s decision boundary and its sensitivity to imaging variations. The clustering step ensures batch-level diversity, while the UIS score promotes the selection of samples beneficial to improve model generalization in single-photon image classification.

3. Experiments and Results

We conducted systematic training and validation of the single-photon active learning network proposed in Section 2.2 on both synthetic datasets and real-world single-photon LiDAR measurement datasets.

3.1. Experiments on the Synthetic Single-Photon Dataset

3.1.1. Experimental Setup

Dastaset: Our synthesized single-photon dataset comprises 11 distinct categories, generated by simulating single-photon measurements from RGB-D images acquired from two different sources: (1) indoor small objects including apple, banana, cap, and water bottle, sourced from the RGB-D Object Dataset [32]; (2) real-world measurements specifically captured using an Intel RealSense Depth Camera D435i, encompassing electric bicycle, garbage bins, traffic barriers, fire hydrants, person, unmanned surface vehicles, and architectural structures. The dataset consists of categories including apples (3,016 samples), bananas (2,908 samples), caps (3150 samples), and water bottles (3,948 samples) obtained from the RGB-D Object Dataset. The parts captured by the depth camera (including electric bicycles, person, unmanned surface vehicles, etc.) contain 250 depth maps and RGB images for each category. The original depth camera captures images at 640×360 resolution. To simulate the low-resolution characteristics of single-photon imaging, we uniformly downsample the pixel resolution by a factor of 5 (128×72). For evaluation, we randomly split each category into training and testing sets, with 70% of the samples used for training and the remaining 30% reserved for testing.

Implementation Details: This paper employs a randomly initialized ResNet-18 model for classification. The model is trained using stochastic gradient descent (SGD) with a momentum of 0.9, an initial learning rate of 0.1, and a batch size of 512 for a total of 200 epochs. A cosine annealing learning rate scheduler is applied during training. Each original sample is augmented by simulating four synthetic variants under diverse imaging conditions (i.e., $M = 4$). Samples are iteratively selected in 7 rounds, each round selecting 50 samples, resulting in a total labeling budget of 350 samples. The candidate pool size for active learning is set to $N_{cand} = 500$ to ensure each cluster contains an average of more than 20 samples. All experiments are repeated three times, and both the average accuracy and standard deviation are reported. Experiments were conducted on an NVIDIA GeForce RTX 4090 GPU.

Baseline: The baseline methods include (1) Entropy, which selects samples with the highest predictive entropy [24], (2) Margin, which selects samples with the smallest margin between the top two predicted class probabilities [25], (3) Coreset, which selects samples whose features are farthest from those of the currently labeled set [26]), and (4) BADGE, which selects samples by performing k-means++ clustering in the gradient embedding space to simultaneously account for uncertainty and diversity [27].

3.1.2. Evaluation Metrics

To elucidate the impact of different MSPPP configurations on the uncertainty of single-photon images, we define the following metrics, the Root Mean Square Error (RMSE) and the Structural Similarity Index (SSIM):

$$\text{RMSE} = \sqrt{\frac{1}{N} \sum_{i=1}^N (d_i - \hat{d}_i)^2}, \quad (12)$$

$$\text{SSIM}(x, y) = \frac{(2\mu_x\mu_y + c_1)(2\sigma_{xy} + c_2)}{(\mu_x^2 + \mu_y^2 + c_1)(\sigma_x^2 + \sigma_y^2 + c_2)}, \quad (13)$$

where d_i represents the deep ground truth, \hat{d}_i denotes the predicted value, and N is the total number of pixels, μ_x and μ_y are the mean values, σ_x and σ_y are the variances, σ_{xy} is the covariance, c_1 and c_2 are constants for computational stability.

To evaluate the performance of the proposed model, the following academic evaluation metrics are formally defined:

$$\text{Accuracy} = \frac{TP + TN}{TP + TN + FP + FN} \times 100\%, \quad (14)$$

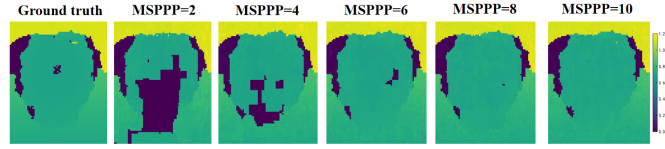
$$\text{Precision} = \frac{TP}{TP + FP} \times 100\%, \quad (15)$$

$$\text{Recall} = \frac{TP}{TP + FN} \times 100\%, \quad (16)$$

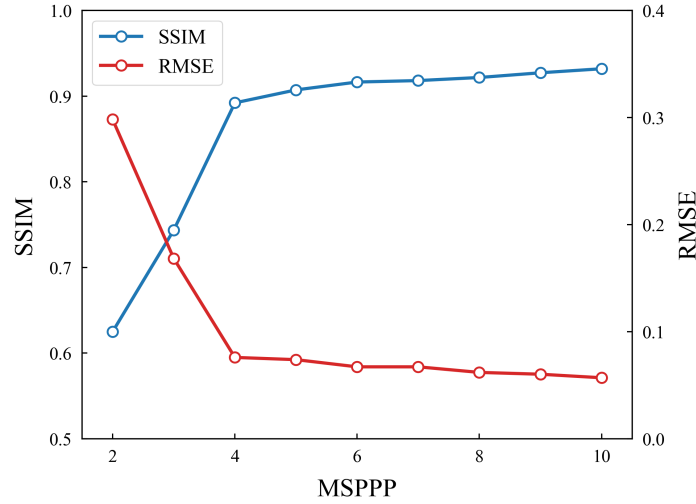
$$\text{F1 Score} = 2 \times \frac{\text{Precision} \times \text{Recall}}{\text{Precision} + \text{Recall}}, \quad (17)$$

where TP (True Positive) represents the number of correctly predicted positive samples, FP (False Positive) indicates the number of negative samples incorrectly predicted as positive, FN (False Negative) denotes the number of actual positive samples incorrectly predicted as negative, and TN (True Negative) represents the number of correctly predicted negative samples.

3.1.3. Multi-Condition Single-Photon Images



(a)



(b)

Fig. 3. Impact of MSPPP on synthetic single-photon imaging quality: (a) visual reconstruction results and (b) RMSE and SSIM analysis.

We present a qualitative comparison between the reconstructed single-photon images produced by our SIV module and the ground-truth depth references. Figure 3a compares image quality under varying MSPPP conditions, while Figure 3b reports the corresponding RMSE and SSIM metrics

with respect to the ground truth. As shown in Figure 3, severe reconstruction artifacts—such as incomplete spatial structures and loss of fine details—appear under extremely low MSPPP levels due to dominant photon-starved noise and degraded spatiotemporal correlations.

3.1.4. Baseline Comparison

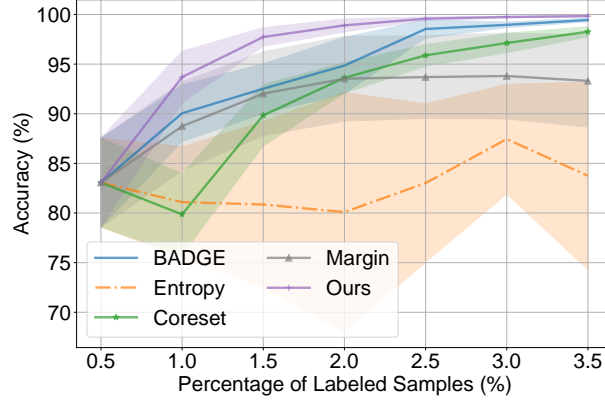


Fig. 4. Performance comparison of active learning strategies in single-photon image classification tasks. The x-axis represents the number of labeled samples, and the y-axis shows the test set classification accuracy. The plot compares the performance differences among, uncertainty sampling (Margin), diversity strategy (Coreset), hybrid method (BADGE), and the proposed DUIS strategy (Ours). The shaded areas represent standard deviations derived from three trials.

Figure 4 shows the classification accuracy of different active learning strategies as the number of labeled samples increases. Overall, all methods exhibit a clear upward trend in accuracy with more labeled data. Notably, all methods except entropy-based sampling surpass 95% accuracy with only 3.5% of the data labeled, suggesting that a relatively small number of annotations can already yield strong performance. This may be attributed to two factors: (1) limited diversity within the synthetic dataset, and (2) the training and test sets are randomly split from the same distribution, without unseen categories or domain shifts. As a result, models can generalize well with few labels.

Our method consistently outperforms all baselines across the full labeling range. It achieves around 95% accuracy with just 1% of labeled data (Table 1) and surpasses 99% at 2.5% labeling (Table 2). For example, to achieve approximately 97% accuracy, our method requires only 1.5% of the data to be labeled, while BADGE and Coreset require 2.5% and 3.5%, respectively, doubling the labeling cost. Entropy-based sampling performs the worst overall, exhibiting both higher variance and lower mean accuracy. The shaded regions in the plot show standard deviation across three runs, where our method also demonstrates superior robustness with the narrow error bands.

The performance advantage of our method stems from two key limitations in existing baselines. First, all baseline methods estimate sample informativeness based only on a single observed image. However, due to the stochastic nature of single-photon imaging, the same scene can appear differently under varying conditions such as photon count or signal-to-background ratio. As a result, a sample that appears confidently predictable under one imaging condition may become highly uncertain under another. Estimating informativeness without accounting for this variability limits the ability of these methods to reliably identify informative samples. Second, methods based on prediction margin or entropy often assign similarly high uncertainty scores

to samples with similar appearances, typically from the same class or cluster. In such cases, selecting all of them for annotation is inefficient, as improving model performance for these samples requires only a few representative examples. The remaining labeling budget could be better spent on diverse samples from other regions or categories. However, these methods do not account for diversity during selection, which leads to redundant sampling and less efficient use of annotation resources.

Table 1. Performance Comparison of Active Learning Strategies at 100 Labeled Samples (approximately 1% of the dataset) on the Synthetic Datasets

Method	Accuracy(%)	Precision (%)	Recall(%)	F1 Score(%)
Entropy	81.09	59.49	64.37	59.30
Margin	88.74	56.34	61.11	56.59
Coreset	79.87	77.97	78.91	77.28
BADGE	90.05	62.03	62.58	59.06
Ours	93.70	80.03	82.04	79.98

Table 2. Performance Comparison of Active Learning Strategies at 250 Labeled Samples (approximately 2.5% of the dataset) on the Synthetic Datasets

Method	Accuracy(%)	Precision (%)	Recall(%)	F1 Score(%)
Entropy	83.02	70.76	72.62	69.66
Margin	93.69	63.12	67.01	63.08
Coreset	95.88	96.94	96.13	96.21
BADGE	98.54	93.02	94.13	93.25
Ours	99.58	98.29	98.14	98.19

Our method addresses both issues. To tackle the challenge of imaging-condition sensitivity, we generate synthetic variants for each sample under different conditions and prioritize those where the model exhibits both high uncertainty and prediction inconsistency. To ensure sample diversity, we incorporate a clustering-based strategy that selects representative samples from different regions of the feature space, thereby improving annotation efficiency across the dataset.

Figure 5 illustrates the t-SNE visualization of feature representations learned using 100 labeled samples. Compared to margin-based sampling (Figure 5c), our method (Figure 5b) produces predictions that more closely align with the true label distribution (Figure 5a), with clearer semantic separation between classes. Moreover, the labeled samples selected by our method (indicated by star markers) are more evenly distributed across the feature space, suggesting better coverage of diverse regions. This supports the effectiveness of our strategy in selecting representative and informative samples for training.

3.2. Experiments on the Real-World Single-Photon Dataset

3.2.1. System and Experiment Description

System Description: Our single-photon LiDAR system employs a 1550nm laser source, generating 1.5 ns ultra-narrow optical pulses while synchronously outputting Transistor-Transistor Logic (TTL) trigger signals at a 1MHz repetition rate. The system’s control architecture utilizes an FPGA as the central controller, which synchronously drives dual acoustic-optic modulators (AOMs), a MEMS mirror, and a high-precision time-to-digital converter (TDC). The time measurement module uses laser TTL signals as start triggers and single-photon avalanche

diode (SPAD) pulses as stop triggers, achieving flight time measurement with 15ps timing jitter and 10MSPS conversion rate, while outputting 4-byte timestamps. The photodetection module incorporates a QuantumCTek QCD600C InGaAs/InP SPAD device, which features active quenching-recovery circuit design, demonstrating 26.5% photon detection efficiency with 2.2 kHz dark count rate. The intrinsic 125 ps timing jitter, combined with laser pulse broadening and TDC quantization error through root-sum-square calculation, ultimately results in 520 ps system-level timing jitter. The spatial scanning system employs a 3 mm aperture MEMS mirror achieving μ rad-level angular resolution through FPGA-generated PWM signals, with maximum mechanical rotation angle of 4.5 degrees. The MEMS mirror's dwell time per pixel is set to approximately $50\mu s$, with each frame's spatial resolution configured at 64×64 pixels and temporal resolution set to 100 ps per pixel. The system achieves approximately 10 cm depth resolution with a maximum imaging range of about 120 meters. The overall system configuration is illustrated in Figure 6.

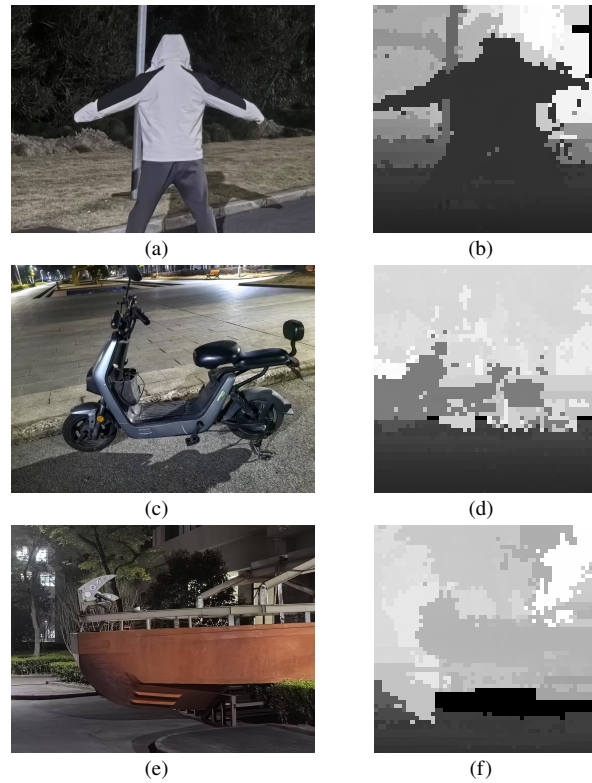


Fig. 7. Data acquired by single-photon LiDAR (person, electric bicycle, unmanned surface vessel), where (a), (c), (e) represent RGB images and (b), (d), (f) are their corresponding single-photon images.

Real-world Single-photon Dataset: We collected single-photon raw data spanning 11 object categories (pedestrian, electric scooter, unmanned surface vessel, etc.) that precisely matched the geometric configurations of synthetic data. Each category contained 100 photon-counting frames captured under three distinct poses, yielding a comprehensive dataset of 1,100 single-photon images. The detection distances (10-100 m) were dynamically adjusted according to the physical dimensions of targets. The acquired raw data was directly fed into the SSPI [31] network for

imaging reconstruction, generating single-photon images at 64×64 resolution. Figure 7 presents a subset of the collected data. For evaluation, we randomly split each category into training and testing sets, with 70% of the samples used for training and the remaining 30% reserved for testing.

Implementation Details: For experiments on the second dataset, we keep the implementation details identical, except that samples are iteratively selected in 10 rounds, each selecting 20 samples. The candidate pool size for active learning is set to $N_{cand} = 40$ to ensure that each cluster contains an average of more than 20 samples.

3.2.2. Experimental Results and Analysis

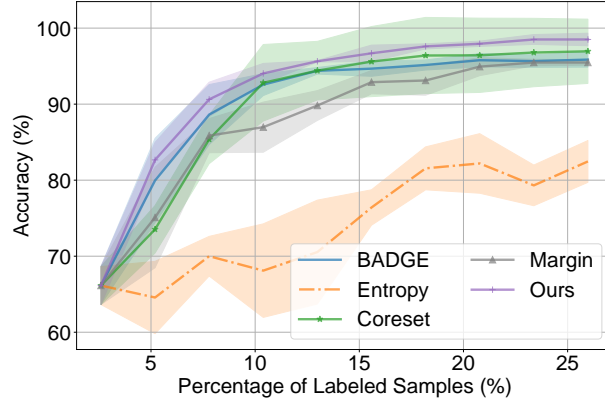


Fig. 8. Performance comparison of active learning strategies in single-photon image classification tasks. The x-axis represents the number of labeled samples, and the y-axis shows the test set classification accuracy. The plot compares the performance differences among uncertainty sampling (Entropy, Margin), diversity strategy (Coreset), hybrid method (BADGE), and the proposed DUIS strategy (Ours). The shaded areas represent standard deviations derived from three trials.

Figure 8 shows the performance of various active learning methods on the real-world single-photon dataset. Due to the dataset’s smaller overall size, the labeled sample percentages appear relatively large; nonetheless, our method consistently outperforms all baselines across the entire annotation range. With only 60 labeled samples (approximately 8% of the dataset), it achieves 90.63% accuracy, which is 4.51% higher than the best-performing baseline (Table 3). These results show trends consistent with those observed on the synthetic dataset, further confirming the effectiveness of our method in reducing annotation cost.

Moreover, our method continues to improve with additional annotations. When the labeled samples increases from 15% to 25% (Table 4), our method shows a consistent accuracy gain, from 96.68% to 97.94%, whereas baseline methods tend to plateau. This further validates the effectiveness of incorporating imaging-condition-aware uncertainty and inconsistency in guiding sample selection.

4. Conclusion

This study addresses the fundamental challenge of semantic interpretation for quantum detection data in extreme environments by developing an active learning framework tailored for single-photon LiDAR imaging. Compared to existing active learning strategies, our proposed method achieves superior classification performance while significantly reducing annotation effort.

Table 3. Performance Comparison of Active Learning Strategies at 60 Labeled Samples (approximately 8% of the dataset) on the Real-Word Datasets

Method	Accuracy(%)	Precision (%)	Recall(%)	F1 Score(%)
Entropy	70.00	68.73	70.00	67.97
Margin	85.86	87.93	85.86	84.26
Coreset	85.38	86.92	85.38	84.49
BADGE	88.63	91.25	88.63	87.58
Ours	90.63	92.28	90.63	90.43

Table 4. Performance Comparison of Active Learning Strategies at 160 Labeled Samples (approximately 21% of the dataset) on the Real-Word Datasets

Method	Accuracy(%)	Precision (%)	Recall(%)	F1 Score(%)
Entropy	82.20	84.42	82.20	81.70
Margin	94.93	95.45	94.93	94.91
Coreset	96.42	97.29	96.43	95.91
BADGE	95.78	96.41	95.78	95.73
Ours	97.94	98.13	97.94	97.95

Specifically, we leverage the impact of MMSSP on single-photon image quality to guide robust uncertainty and inconsistency estimation. Driven by this comprehensive uncertainty metric, our approach efficiently identifies and annotates the most informative samples. Extensive experiments on both synthetic and real-world datasets demonstrate that our method outperforms state-of-the-art active learning techniques in classification accuracy while requiring substantially fewer labeled samples.

Disclosures. The authors declare that there are no conflicts of interest related to this article.

References

1. R. H. Hadfield, "Single-photon detectors for optical quantum information applications," *Nat. Photonics* **3**, 696–705 (2009).
2. J. J. Degnan, "Unified approach to photon-counting microlaser rangefinders, transponders, and altimeters," *Surv. Geophys.* **22**, 431–447 (2001).
3. A. McCarthy, G. G. Taylor, J. Garcia-Armenta, *et al.*, "High-resolution long-distance depth imaging lidar with ultra-low timing jitter superconducting nanowire single-photon detectors," *Optica* **12**, 168–177 (2025).
4. J. Rapp and V. K. Goyal, "A few photons among many: Unmixing signal and noise for photon-efficient active imaging," *IEEE Trans. on Comput. Imaging* **3**, 445–459 (2017).
5. A. Halimi, R. Tobin, A. McCarthy, *et al.*, "Robust restoration of sparse multidimensional single-photon lidar images," *IEEE Trans. on Comput. Imaging* **6**, 138–152 (2019).
6. J. Tachella, Y. Altmann, N. Mellado, *et al.*, "Real-time 3D reconstruction from single-photon lidar data using plug-and-play point cloud denoisers," *Nat. Commun.* **10**, 4984 (2019).
7. Z. P. Li, J. T. Ye, X. Huang, *et al.*, "Single-photon imaging over 200 km," *Optica* **8**, 344–349 (2021).
8. R. Tobin, A. Halimi, A. McCarthy, *et al.*, "Three-dimensional single-photon imaging through obscurants," *Opt. Express* **27**, 4590–4611 (2019).
9. J. J. Degnan, "Scanning, multibeam, single photon lidars for rapid, large scale, high resolution, topographic and bathymetric mapping," *Remote. Sens.* **8**, 958 (2016).
10. J. Rapp, J. Tachella, Y. Altmann, *et al.*, "Advances in single-photon lidar for autonomous vehicles: Working principles, challenges, and recent advances," *IEEE Signal Process. Mag.* **37**, 62–71 (2020).
11. Y. Hong, S. Liu, Z. P. Li, *et al.*, "Airborne single-photon lidar towards a small-sized and low-power payload," *Optica* **11**, 612–618 (2024).
12. M. Shangguan, Z. Yang, M. Shangguan, *et al.*, "Remote sensing oil in water with an all-fiber underwater single-photon raman lidar," *Appl. Opt.* **62**, 5301–5305 (2023).
13. A. Kirmani, D. Venkatraman, D. Shin, *et al.*, "First-photon imaging," *Science* **343**, 58–61 (2014).

14. J. Tachella, Y. Altmann, X. Ren, *et al.*, “Bayesian 3D reconstruction of complex scenes from single-photon lidar data,” *SIAM J. on Imaging Sci.* **12**, 521–550 (2019).
15. Q. Legros, S. Meignen, S. McLaughlin, and Y. Altmann, “Expectation-maximization based approach to 3D reconstruction from single-waveform multispectral lidar data,” *IEEE Trans. on Comput. Imaging* **6**, 1033–1043 (2020).
16. R. H. Hadfield, J. Leach, F. Fleming, *et al.*, “Single-photon detection for long-range imaging and sensing,” *Optica* **10**, 1124–1141 (2023).
17. Z. Li, H. Pan, G. Shen, *et al.*, “Single-photon lidar for canopy detection with a multi-channel Si SPAD at 1064 nm,” *Opt. & Laser Technol.* **157**, 108749 (2023).
18. Z.-M. Li, H. Zhou, Z.-Y. Li, *et al.*, “Thresholded single-photon underwater imaging and detection,” *Opt. Express* **29**, 28124–28133 (2021).
19. J. Deng, W. Dong, R. Socher, *et al.*, “Imagenet: A large-scale hierarchical image database,” in *2009 IEEE Conference on Computer Vision and Pattern Recognition*, (IEEE, 2009), pp. 248–255.
20. X. Li, J. Liu, G. Zhao, *et al.*, “High precision single-photon object detection via deep neural networks,” *Opt. Express* **32**, 37224–37237 (2024).
21. G. MoraMartin, S. Scholes, R. K. Henderson, *et al.*, “Human activity recognition using a single-photon direct time-of-flight sensor,” *Opt. Express* **32**, 16645–16656 (2024).
22. Y. Gal, R. Islam, and Z. Ghahramani, “Deep bayesian active learning with image data,” in *International Conference on Machine Learning*, (PMLR, 2017), pp. 1183–1192.
23. P. Ren, Y. Xiao, X. Chang, *et al.*, “A survey of deep active learning,” *ACM Comput. Surv. (CSUR)* **54**, 1–40 (2021).
24. D. D. Lewis and J. Catlett, “Heterogeneous uncertainty sampling for supervised learning,” in *Machine Learning Proceedings 1994*, (Elsevier, 1994), pp. 148–156.
25. T. Scheffer, C. Decomain, and S. Wrobel, “Active hidden markov models for information extraction,” in *International Symposium on Intelligent Data Analysis*, (Springer, 2001), pp. 309–318.
26. O. Sener and S. Savarese, “Active learning for convolutional neural networks: A core-set approach,” in *International Conference on Learning Representations*, (ICLR, 2018).
27. J. T. Ash, C. Zhang, A. Krishnamurthy, *et al.*, “Deep batch active learning by diverse, uncertain gradient lower bounds,” in *International Conference on Learning Representations*, (ICLR, 2020).
28. J. Li, C. Wang, T. Chen, *et al.*, “Deep learning-based quantitative optoacoustic tomography of deep tissues in the absence of labeled experimental data,” *Optica* **9**, 32–41 (2022).
29. Y. Xue, S. Cheng, Y. Li, and L. Tian, “Reliable deep-learning-based phase imaging with uncertainty quantification,” *Optica* **6**, 618–629 (2019).
30. D. Shin, A. Kirmani, V. K. Goyal, and J. H. Shapiro, “Photon-efficient computational 3D and reflectivity imaging with single-photon detectors,” *IEEE Trans. on Comput. Imaging* **1**, 112–125 (2015).
31. G. Yao, Y. Chen, C. Jiang, *et al.*, “Dynamic single-photon 3D imaging with a sparsity-based neural network,” *Opt. Express* **30**, 37323–37340 (2022).
32. K. Lai, L. Bo, X. Ren, and D. Fox, “A large-scale hierarchical multi-view RDB-D object dataset,” in *2011 IEEE International Conference on Robotics and Automation*, (IEEE, 2011), pp. 1817–1824.